Journal of Energy Storage 180 (2026) 124080

Contents lists available at ScienceDirect

Journal of Energy Storage

journal homepage: www.elsevier.com/locate/est

Research Papers

Benchmarking of multi-order equivalent-circuit models with empirical ageing for Li-ion battery digital-twin workflows

Sara Carcangiu, Santhosh Paramasivam, Amit Kumar *, Fabrizio Pilo, Gianluca Gatto

Department of Electrical and Electronic Engineering, University of Cagliari, via Marengo 2, 09123, Cagliari, Italy

ARTICLE INFO

Keywords:
Battery ageing
Battery management systems (BMS)
Digital-twin workflow
Equivalent-circuit models
Lithium-ion batteries
Model benchmarking
State of health

ABSTRACT

Accurate and computationally efficient battery models are essential for battery management systems and battery digital-twin workflows. However, model selection requires careful evaluation of the trade-off between dynamic voltage fidelity, computational effort, energy accounting, and ageing representation. This paper presents a reproducible MATLAB-based benchmarking workflow for comparing equivalent-circuit models (ECMs) at battery-pack scale under common parameterisation and ageing assumptions. A SAFT-type RC model and first-, second-, and third-order Thevenin models are evaluated using open-access state of charge (SoC)/state of health (SoH)-dependent parameter surfaces, an empirical calendar–cycling ageing law, and automated post-processing through the DATTES toolbox. The benchmark is performed on a 64s29p $LiFePO_4$ battery pack under a repeated synthetic 24-h current profile over a three-year equivalent operating horizon at fixed 25 °C. The results show that higher-order ECMs improve agreement with the third-order Thevenin internal reference, but the incremental benefit diminishes beyond the second-order model. Within the investigated model family, duty cycle, and MATLAB implementation, the second-order Thevenin model provides the most favourable compromise between internal-reference voltage fidelity and per-step computational cost. The ageing outputs show identical SoH and internal-resistance-growth trajectories across ECMs because the adopted ageing law is driven by common daily stress metrics rather than ECM-specific polarization states or transient overpotential histories. Therefore, these ageing results should be interpreted as a property of the implemented modular ageing-coupling strategy, not as a general proof that ECM order has no influence on degradation in real batteries. The study provides a transparent and reproducible benchmarking workflow for controlled ECM comparison, while experimental validation, electro-thermal coupling, and estimator-in-the-loop testing remain necessary before predictive deployment in operational BMS or digital-twin systems.

1. Introduction

The global transition toward sustainable mobility, distributed energy storage, and large-scale electrification has increased the demand for accurate, interpretable, and computationally efficient models of lithium-ion (Li-ion) batteries. In electric vehicles, hybrid systems, and stationary storage applications, battery management systems (BMS) must estimate and control internal states such as State of Charge (SoC), State of Health (SoH), available power, and degradation under dynamic operating conditions. Recent reviews highlight that model fidelity directly impacts safety, lifetime prediction, and energy management in electric-vehicle and grid-connected applications [1,2]. At the same time, embedded BMS and battery digital-twin workflows require models that remain numerically robust and computationally tractable over long operating horizons [1,3].

Among the available modelling approaches, equivalent-circuit models (ECMs) remain widely used because they offer a favourable balance between physical interpretability and computational efficiency. Charge-based formulations, such as SAFT-type RC networks, provide a compact representation of surface–bulk charge redistribution, whereas voltage-based Thevenin models describe polarization dynamics through one or more RC branches. Foundational ECM formulations by Chen and Rincón-Mora [4] and Tremblay and Dessaint [5] established compact nonlinear models suitable for control-oriented simulation. Subsequent experimental and simulation-based comparisons by He et al. [6] and Hu et al. [7] showed that first- and second-order Thevenin models often provide favourable accuracy–complexity trade-offs for voltage modelling and state estimation. More recent surveys on parameter estimation and ECM usage confirm that these model families continue to form the

* Corresponding author.
E-mail address: amit.kumar@unica.it (A. Kumar).

https://doi.org/10.1016/j.est.2026.124080
Received 5 March 2026; Received in revised form 15 July 2026; Accepted 10 August 2026

Nomenclature

Abbreviations

BMS	Battery management system
DATTES	Data Analysis Tools for Tests on Energy Storage
DoD	Depth of discharge
ECM	Equivalent-circuit model
EoL	End of Life
FEC	Full equivalent cycles
LFP	Lithium iron phosphate ($LiFePO_4$)
NRMSE	Normalised root-mean-square error
OCV	Open-circuit voltage
PDE	Partial differential equation
RC	Resistor–Capacitor (SAFT-type dual-capacitor model)
RC–SAFT	SAFT-type resistor-capacitor surface-bulk charge-redistribution model
RMSE	Root-mean-square error
SoC	state of charge
SoH	state of health
SoH_{surf}	SoH coordinate used for parameter-surface interpolation
Th1, Th2, Th3	First-, second-, third-order Thevenin model
TVE	Total vector error
ZOH	Zero-order hold
pp	percentage points

Latin symbols

A_{cal}	Calendar-ageing pre-exponential factor [day^{-1}]
a, b	Empirical SoC-dependence coefficients of calendar ageing
C_b	Bulk-domain capacitance [F]
C_c	Surface-domain capacitance [F]
C_i	Capacitance of the i-th polarization branch, $i = 1,2,3$ [F]
C_n	Nominal capacity, updated with SoH [Ah]
C_{tot}	Total electrochemical capacitance [F]
E_a	Activation energy of calendar ageing [J mol^{-1}]
E_{in}, E_{out}	Daily charge / discharge energy [Wh]
I	Terminal current, positive in discharge [A]
I_b, I_c	Bulk / surface branch currents [A]
k_{cal}	Calendar degradation rate [day^{-1}]
k_{cyc}	Cycle degradation coefficient [% $cycle^{-1}$]
$k_{cyc,scale}$	Multiplicative scale factor applied to the cycling-loss term in the ageing sensitivity analysis
k_{rint}	Resistance-growth proportionality factor [%]
M_{rel}	Relative static storage index
Mid-SoC	Mean state of charge over the daily cycle [%]
N_{cycles}	Full equivalent cycles in a day
N_s, N_p	Number of series / parallel cells (64s29p)
n_p	Thevenin model order (1, 2, 3)
Q_{nom}	Nominal charge [C]
R	Universal gas constant, 8.314 J mol^{-1} K^{-1}
R_0	Series resistance of the Thevenin models equivalent to R_{int} [Ω]
R_c	Interfacial resistance, lumped into R_{int} [Ω]
R_e	Coupling (exchange) resistance, surface–bulk [Ω]
R_i	Resistance of the i-th polarization branch [Ω]
R_{int}	Terminal ohmic (internal) resistance [Ω]
T	Absolute temperature [K]
T_{cycle}, $T_{storage}$	Cycling / storage temperature [°C]
T_s	Sampling period [s] ($T_s = 60s$)
$t_{storage}$	Rest (storage) time [days]
V	Terminal voltage [V]
V_b	Bulk-domain voltage [V]
V_c	Surface overpotential [V]
V_{OC}	Open-circuit voltage [V]
V_{p_i}	Polarization voltage of the i-th branch [V]
x	Model state vector

Greek symbols

α	RC–SAFT capacity-splitting factor, $C_c/(C_c + C_b)$; baseline $\alpha = 0.20$
α_i	Exponential-filter coefficient, $\alpha_i = \exp\left(\frac{-T_s}{R_i C_i}\right)$
ΔC_{cal}, ΔC_{cyc}	Daily calendar / cycling capacity loss [%]
ΔC_{day}	Total daily capacity loss [%]
ΔR_{int}	Cumulative internal-resistance growth [%]
ΔV_{ref}	Reference voltage swing used for C_tot [V]
η	Coulombic efficiency
η_{charge}	Charge-side coulombic efficiency used in the synthetic profile definition
η_{day}	Daily round-trip efficiency [%]
ρ_P	Pearson correlation coefficient used in Section 3.7
ρ_S	Spearman rank-correlation coefficient used in Section 3.9
ρ_w	Current-weighted Spearman rank-correlation coefficient used in Section 3.9
σ	Standard deviation of the Gaussian standby-current perturbation [A]
τ	Time constant [s]
τ_k	Kendall rank-correlation coefficient used in Section 3.9
τ_w	Current-weighted Kendall coefficient used in Section 3.9
τ_1	Time constant of the first polarization branch, R_1C_1 [s]
τ_{cal}	Local calendar lifetime [days]
τ_{min}, τ_{max}	Admissible bounds on the RC–SAFT diffusion time constant [s]

backbone of modern BMS implementations [8].

The selected ECM structure also affects the performance of state-estimation algorithms. Reviews on SoC and SoH estimation show that estimator robustness, convergence speed, and numerical stability are inherently constrained by the observability and identifiability properties of the underlying model [9–12]. Waag et al. [13] highlighted the risk of estimator degradation under controlled scenario-based operating conditions when the model structure is not appropriate, while Berecibar et al. [14] and Barillas et al. [15] stressed the importance of consistent model parameterisation for meaningful comparison of estimation algorithms. Classical Extended Kalman Filtering developments for Li-ion battery packs [16–18] and subsequent robustness studies [19] further illustrate the central role of ECM quality in model-based estimation. Recent applications continue to rely on Thevenin-type ECMs for real-time SoC estimation and BMS implementation [20], even as hybrid physics–machine learning methods are increasingly explored for improved state estimation under variable operating and ageing conditions [21].

In parallel, substantial progress has been made in Li-ion battery ageing mechanisms and lifetime prediction. Recent reviews summarise degradation mechanisms such as capacity fade, internal-resistance growth, and open-circuit voltage drift, and highlight the need for ageing-aware models suitable for system-level analysis [2,3]. Long-term experimental datasets, including the multi-stage ageing dataset reported by Stroebl et al. [22], provide valuable references for degradation-model validation, while second-life ageing studies further emphasise the need to represent ageing beyond first-life operation [23].

Open-data initiatives have also enabled combining empirical ageing laws with experimentally derived parameter surfaces. The Batteries2020 project introduced empirically validated calendar-plus-cycling ageing laws suitable for long-term simulations [24]. Seger et al. released open ageing models and SoC–SoH-dependent ECM parameter surfaces for

second-life lithium-ion batteries [25,26]. In addition DATTES (Data analysis tools for tests on energy storage) provides standardised tools for battery data analysis and reproducible post-processing [27], while recent digital-twin architectures illustrate the growing interest in integrating battery models, data streams, and analytics for battery-state awareness [28,29].

Although ECMs, ageing laws, open-parameter datasets, and battery-data analysis tools have each been investigated independently, their integration into a transparent, reproducible workflow for long-horizon, pack-level model comparison remains limited. In particular, controlled benchmarking studies are needed to evaluate how ECM family and order affect voltage response, energy throughput, round-trip efficiency, degradation indicators, and computational effort under identical parameterisation and ageing assumptions. This need is especially relevant for BMS development and digital-twin-oriented workflows, where model fidelity must be balanced against numerical stability, implementation cost, and reproducibility. Recent work on electro-thermal pack modelling, real-time BMS control, and ageing-aware battery simulation further confirms the practical importance of this balance [30–32].

It is important to clarify that the objective of the present work is not to introduce a new ECM topology or to establish the general superiority of a specific Thevenin order. Previous studies have already shown that first- and second-order Thevenin models often provide favourable accuracy–complexity trade-offs for battery modelling and state estimation [6,7]. Instead, the contribution of this work lies in integrating established model structures, open SoC–SoH-dependent parameter surfaces, an empirical calendar–cycling ageing formulation, and standardised post-processing into a single MATLAB-based benchmarking workflow. This enables a controlled and reproducible comparison of model-family behaviour under identical operating, parameterisation, and ageing assumptions.

The main contributions of this work are as follows:

- A reproducible MATLAB workflow is developed for benchmarking a SAFT-type RC model and first-, second-, and third-order Thevenin ECMs at battery-pack scale.
- A common parameterisation procedure is implemented using open SoC–SoH-dependent parameter surfaces with explicit boundary handling for the available second-life SoH domain, allowing consistent comparison across model families and orders [25,26].
- An empirical calendar–cycling ageing update is coupled to the ECM simulation workflow to support long-horizon scenario analysis under common degradation assumptions [24].
- Automated post-processing is performed using the DATTES toolbox to evaluate voltage response, energy throughput, round-trip efficiency, degradation indicators, and computational performance [27].
- A scenario-specific comparison is conducted for a 64s29p $LiFePO_4$ battery pack under fixed-temperature operation and a repeated synthetic 24-h current profile over a three-year equivalent horizon.

The scope of the study is intentionally defined as a model-based benchmarking exercise. The results quantify the relative behaviour of the tested ECM configurations within the adopted parameter surfaces, ageing law, current profile, pack configuration, and MATLAB implementation. They should not be interpreted as experimental validation of absolute voltage accuracy, efficiency, or degradation prediction for a real battery pack. Experimental validation against measured dynamic current–voltage data, electro-thermal coupling, multi-chemistry testing, and estimator-in-the-loop implementation are identified as necessary extensions before predictive BMS or operational digital-twin deployment.

The remainder of the paper is organised as follows. Section 2 describes the ECM formulations, parameterisation procedure, ageing coupling, simulation workflow, and reproducibility considerations. Section 3 presents result on voltage, energy, ageing, computational performance, and fidelity. Section 4 summarises the main findings, limitations, and future extensions of the proposed benchmarking workflow.

2. Modelling framework and methodology

2.1. Framework overview and simulation workflow

This study proposes a unified simulation framework that integrates SAFT-type RC and multi-order Thevenin equivalent-circuit models (ECMs) with an empirical ageing module and automated post-processing via the DATTES toolbox. The platform is designed to simulate lithium-ion battery ECMs under a controlled synthetic 24-h current profile designed for controlled benchmarking, capturing both short-term dynamics and long-term degradation. Each simulation run covers a 24-h current profile that includes moderate and high-power discharge phases, constant-current and fast charging segments, and idle periods. This daily profile is repeated over a three-year equivalent operating horizon using a fixed 60-s sampling interval, resulting in approximately 1.5 million time steps.

Parallel execution enables the simultaneous evaluation of multiple ECM families and model orders, facilitating direct comparisons in terms of dynamic fidelity, computational efficiency, and degradation trends. The overall workflow, ranging from parameter initialization to standardised post-analysis, is summarised in Fig. 1.

2.2. Equivalent-circuit models

This study implements four equivalent-circuit model (ECM) configurations, grouped into two distinct families: a SAFT-inspired RC topology describing bulk–surface charge redistribution, and first-, second-, and third-order Thevenin models capturing voltage-based polarization dynamics.

The RC model adopts a dual-capacitor topology originally developed by SAFT for vehicle-level simulations [6]. The classical network includes two capacitors C_c, C_b and three resistors: the terminal resistance R_{int}, a coupling resistance R_e, and an interfacial resistance R_c.

In this work, we adopt a reduced 2C–2R formulation (Fig. 2) where R_c is lumped into the terminal ohmic resistance R_{int}, whose SoC–SoH dependence is taken from the same interpolation surfaces used for the Thevenin models, and the coupling resistance R_e governs charge exchange between the surface and bulk domains. All resistances and voltages are defined with respect to the open-circuit voltage (OCV) node.

In this phenomenological framework:

- The surface domain represents fast interfacial phenomena (e.g., double-layer capacitance, charge-transfer resistance), modelled via a small capacitor C_c and overpotential V_c;
- The bulk domain captures slower charge redistribution within the porous electrode and active material, using a larger capacitor C_b and voltage V_b;

The coupling resistor R_e mimics diffusion-like relaxation between domains without requiring PDE-based electrochemical models, retaining physical interpretability with low computational cost.

The state vector is $x = [SoC, V_c, V_b]^T$, where SoC $\in [0,1]$ is the normalised state of charge.

The terminal current I is defined positive in discharge, i.e., flowing out of the positive terminal. With this convention, the output voltage equation is

$$V = V_{OC}(SoC) - R_{int}I - V_c \tag{1}$$

The ohmic and surface polarization terms reduce the terminal

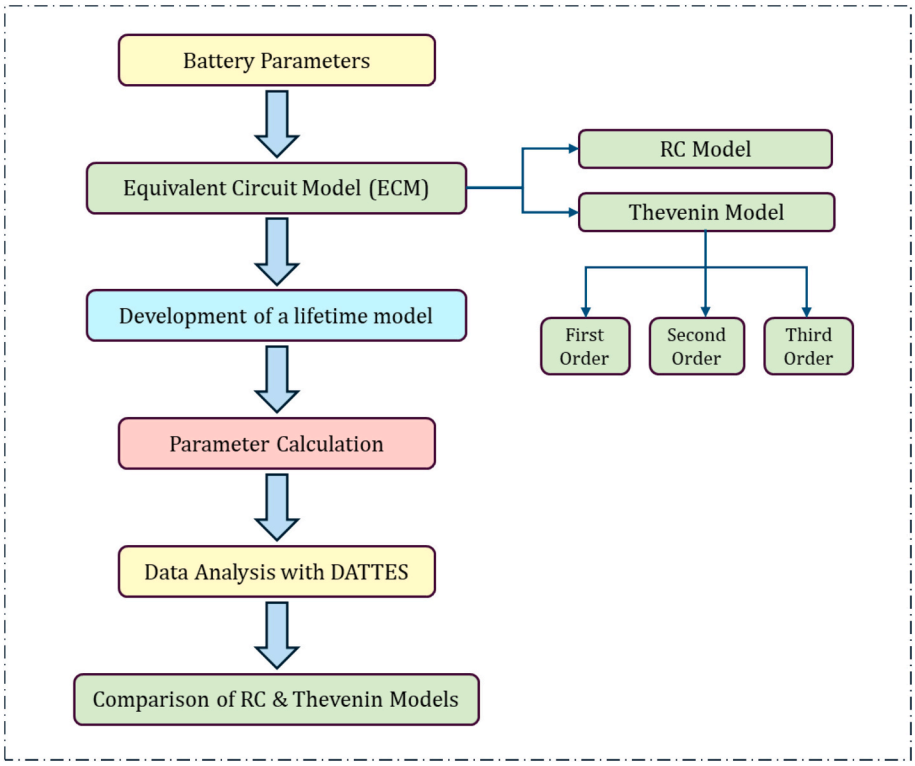

Fig. 1. Overview of the unified simulation framework, from parameter initialization to data analysis and model comparison.

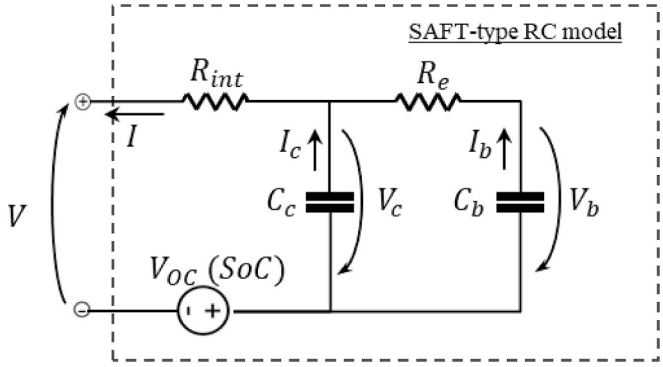

Fig. 2. Schematic of the reduced SAFT-type RC battery model.

voltage during discharge ($I > 0$) and increase it during charge ($I < 0$), consistent with physical behaviour.

The SoC evolution follows Coulomb counting:

$$\frac{dSoC}{dt} = -\frac{\eta I}{3600\, C_n} \tag{2}$$

where η is the coulombic efficiency and C_n the nominal capacity (Ah) updated with SoH.

The inter-domain dynamics are governed by:

$$\frac{dV_c}{dt} = \frac{1}{C_c} I - \frac{1}{C_c R_e}(V_c - V_b),$$

$$\frac{dV_b}{dt} = \frac{1}{C_b R_e}(V_c - V_b). \tag{3}$$

The Thevenin models use voltage-based RC ladder networks to capture multi-time-constant polarization dynamics. Each branch consists of a parallel resistor–capacitor pair $(R_i \parallel C_i)$, which generates a polarization voltage V_{p_i}. Unlike the RC model, Thevenin configurations do not differentiate between bulk and surface domains but offer tunable fidelity via model order:

- Th1: $R_{int} + (R_1 \| C_1)$, capturing a dominant polarization mode.
- Th2: $R_{int} + (R_1 \| C_1) + (R_2 \| C_2)$, resolving medium and slow dynamics.
- Th3: $R_{int} + (R_1 \| C_1) + (R_2 \| C_2) + (R_3 \| C_3)$, offering high-fidelity transient response.

The terminal voltage is given by:

$$V = V_{OC}(SoC) - IR_{int} - \sum_{i=1}^{n_p} \mathrm{V}_{p_i} \tag{4}$$

where $n_p = 1, 2, 3$ denotes the model order.

Each polarization voltage is updated via a first-order exponential filter:

$$V_{p_i,k+1} = \alpha_i V_{p_i,k} + R_i(1-\alpha_i) I_k, \quad \alpha_i = \exp\left(-\frac{T_s}{R_i C_i}\right) \tag{5}$$

The SoC is updated using the same Coulomb-counting equation as in the RC model. This discretization ensures long-term numerical stability across millions of time steps.

A schematic representation of the generalised Thevenin structure is shown in Fig. 3 and Table I summarises the four model structures and their associated state vectors.

To ensure consistency across ECM families, the RC–SAFT model reuses the same V_{OC} and R_{int} surfaces employed in the Thevenin models. Its internal parameters are derived analytically to match the dominant time constant $\tau_1 = R_1 C_1$ of the Th1 configuration, as detailed in Section 2.3.

2.3. Parameterisation and interpolation

The experimentally derived electrical parameters used as the com-

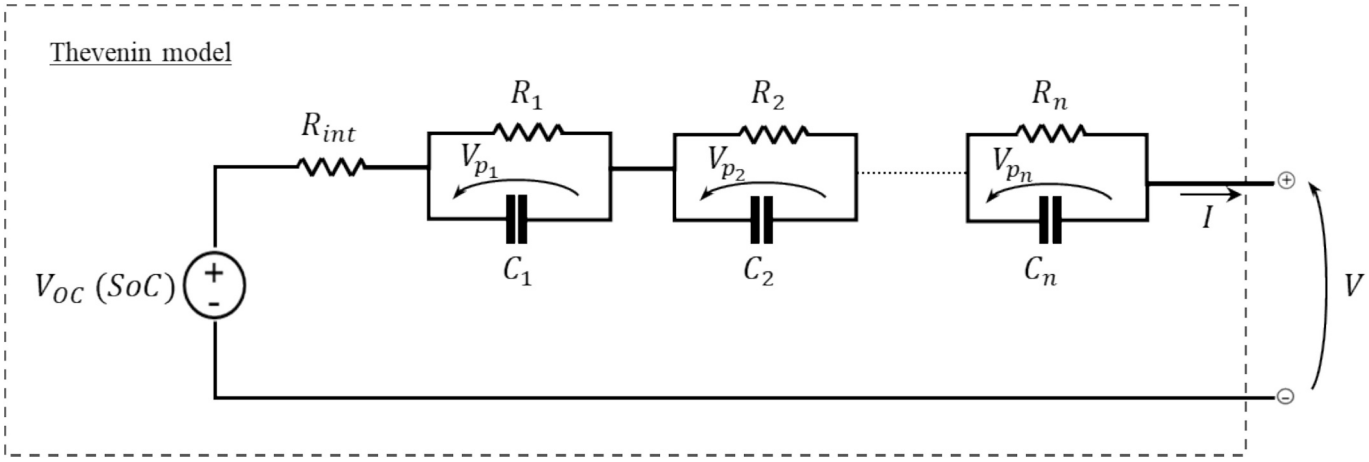

Fig. 3. Generalised Thevenin equivalent-circuit model of order ***n***.

Table I
Model components and state vectors.

Model	Components	State vector $\boldsymbol{x}$
RC–SAFT	R_{int}, R_e, C_c, C_b	[SoC; V_c; V_b]
Thevenin 1st order (Th1)	R_0, R_1, C_1	[SoC; V_{p_1}]
Thevenin 2nd order (Th2)	R_0, R_1, C_1, R_2, C_2	[SoC; V_{p_1}; V_{p_2}]
Thevenin 3rd order (Th3)	$R_0, R_1, C_1, R_2, C_2, R_3, C_3$	[SoC; V_{p_1}; V_{p_2}; V_{p_3}]

mon basis for the equivalent-circuit models are obtained from the open-access parameterisation dataset reported in [26]. The available two-dimensional interpolation surfaces provide the open-circuit voltage V_{OC}, the ohmic resistance R_{int}, and the first two polarization branches (R_1, C_1) and (R_2, C_2) as functions of SoC and state of health. Each surface maps values over the SoC domain (SoC $\in$ [0,1]) and the second-life SoH domain (SoH $\in$ [0.5, 0.8]), with separate datasets for 25 °C and 0 °C and for charge and discharge conditions.

During the simulation, cell-level parameters are extracted at runtime via bilinear interpolation according to the instantaneous SoC, the ageing-dependent SoH coordinate, temperature, and current direction. Since the source parameter surfaces are available only over the second-life SoH interval (SoH $\in$ [0.5, 0.8]), the SoH coordinate used for interpolation is constrained to this admissible range. In the three-year scenario analysed in this work, the simulated physical SoH decreases from 1.00 to approximately 0.835 and therefore remains above the upper bound of the available surface domain. Consequently, the interpolation coordinate is kept at the upper boundary, $\mathrm{SoH_{surf}} = 0.8$, throughout the reported simulations. As a result, V_{OC}, R_1, C_1, R_2, and C_2 are evaluated at the SoH = 0.8 surface, while ageing affects the electrical simulation through the capacity update C_n (SoH) and the empirical internal-resistance-growth update described in Section 2.4. The resulting cell-level parameters are then analytically scaled to the 64s29p pack configuration by applying the corresponding series–parallel resistance, capacitance, and voltage scaling factors.

For the first- and second-order Thevenin configurations, the interpolated internal resistance R_{int} provides the baseline ohmic resistance, while the polarization branches are defined directly by the interpolated (R_i, C_i) pairs. The effective series resistance is then updated according to the empirical resistance-growth formulation described in Section 2.4. The third-order Thevenin configuration is treated as an internal higher-order numerical extension of the same parameterisation framework. Since the source dataset does not provide independently identified R_3 and C_3 surfaces, the third branch is derived analytically from the available second-branch parameters and is used only as an internal higher-order reference within the model-based benchmark, not as an experimentally identified ground truth.

The RC–SAFT model shares the same V_{OC} and R_{int} surfaces used for the Thevenin models, ensuring a common open-circuit-voltage and ohmic-resistance basis. However, no dedicated lookup tables are available for C_c, C_b, or R_e. These quantities are therefore computed analytically so that the reduced surface–bulk charge redistribution dynamics are harmonised with the dominant time scale of the first Thevenin branch.

Specifically, the time constant of the first polarization branch $\tau_1 = R_1 C_1$ is used as a reference diffusion-like timescale. At each simulation step, this value is constrained within a physically admissible interval $[\tau_{\min}, \tau_{\max}]$ to avoid unrealistically fast or slow charge redistribution. For the reduced two-capacitor RC–SAFT model, the surface-bulk redistribution time constant is given by $\tau_{RC} = R_e \frac{C_c C_b}{C_c + C_b}$. Therefore, to harmonise the RC–SAFT redistribution timescale with the first Thevenin time constant, the exchange resistance is selected as:

$$R_e = \tau_1 \frac{C_c + C_b}{C_c C_b} \tag{6}$$

The total electrochemical capacitance is linked to the nominal charge capacity and to a reference voltage swing according to:

$$C_{\mathrm{tot}} = \frac{Q_{\mathrm{nom}}}{\Delta V_{\mathrm{ref}}} \tag{7}$$

where Q_{nom} is the nominal charge expressed in coulombs. The capacitance is then partitioned between the surface and bulk domains as

$$C_c = \alpha C_{\mathrm{tot}}, \qquad C_b = (1-\alpha) C_{\mathrm{tot}}$$

where $\alpha = \frac{C_c}{C_c + C_b}$ is the RC–SAFT capacity-splitting factor. The baseline value $\alpha = 0.20$ was selected to represent a reduced fast surface storage region coupled to a dominant slower bulk reservoir. This choice is consistent with the phenomenological interpretation of the RC–SAFT model, where the surface domain captures fast interfacial charge redistribution, while the bulk domain represents the larger charge-storage contribution.

The parameter α is not treated as an independently identified electrochemical parameter in the present framework. Rather, it is used as a phenomenological capacity-partitioning factor that enables the reduced RC–SAFT model to reproduce a diffusion-like redistribution time scale consistent with the first Thevenin branch. To verify that the benchmarking conclusions are not driven by this choice, a robustness check was carried out by varying α over the range 0.10–0.50 while keeping all other inputs, ageing laws, parameter surfaces, and numerical settings unchanged. The corresponding effect on energy throughput, round-trip efficiency, and voltage response is discussed in Section 3.3.

This parameterisation strategy ensures that all ECMs share the same

open-data basis for V_{OC}, R_{int}, and the available polarization elements, while allowing the RC–SAFT parameters and the third Thevenin branch to be derived without dedicated additional identification. The explicit boundary handling of the SoH coordinate also ensures consistency between the available second-life parameter surfaces and the ageing trajectory simulated in the present benchmark.

2.4. Integration of calendar and cycling ageing models

Lithium-ion battery degradation is modelled using a hybrid ageing law that combines both calendar and cycling mechanisms, following the empirical formulation proposed in [24]. This coupling allows the ECM simulations to account for capacity fade and effective internal-resistance growth over time, reproducing the gradual loss of capacity and the increase in internal resistance under realistic storage and usage conditions.

The rate of capacity fade due to storage is governed by a temperature- and SoC-dependent expression:

$$k_{\mathrm{cal}}(T, SoC) = A_{\mathrm{cal}} \exp\left(-\frac{E_a}{RT}\right) \frac{1}{a + b \cdot SoC} \tag{8}$$

where A_{cal} is the pre-exponential factor (day^{-1}), E_a the activation energy (J mol^{-1}), R the universal gas constant (8.314 J mol^{-1} K^{-1}), T the absolute temperature (K), and a, b are empirical SoC-dependence coefficients.

The resulting daily capacity loss due to calendar ageing is:

$$\Delta C_{\mathrm{cal}} = \frac{t_{\mathrm{storage}}}{\tau_{\mathrm{cal}}(T, \mathrm{SoC})} \tag{9}$$

where $t_{storage}$ is the time spent at rest and $\tau_{cal} = 1/k_{cal}$ is the local calendar lifetime (in days) under given T, SoC conditions. Cycling-induced degradation is modelled as a function of depth of discharge (DoD), mean SoC, and temperature:

$$\Delta C_{\mathrm{cyc}} = N_{\mathrm{cycles}}\ k_{\mathrm{cyc}}(DoD, T, Mid - SoC) \tag{10}$$

where N_{cycles} is the number of full-equivalent cycles in the current day, k_{cyc} is the cycle degradation coefficient evaluated on interpolated maps or fitted surfaces and where $Mid - SoC$ is the mean SoC during the cycle.

Each simulated day, the total capacity fade is computed as:

$$\Delta C_{\mathrm{day}} = \Delta C_{\mathrm{cal}} + \Delta C_{\mathrm{cyc}} \tag{11}$$

and the daily internal-resistance-growth increment is updated according to:

$$\Delta R_{\mathrm{int,day}} = k_{\mathrm{rint}} \cdot \Delta C_{\mathrm{day}} \tag{12}$$

where k_{rint} is an empirical proportionality factor relating internal-resistance growth to capacity loss. The cumulative internal-resistance increase is then obtained by summing the daily increments over the simulated horizon.

In the reported three-year simulations, the ageing update affects the electrical model through two channels: the reduction of the available nominal capacity C_n, used in the SoC update, and the empirical increase of the effective internal resistance through Eq. (12). Since the simulated SoH remains above the upper bound of the available parameter-surface domain, the SoH coordinate used for V_{OC}, baseline R_{int}, and polarization-parameter lookup is clamped at $SoH_{surf} = 0.8$. Therefore, the lookup-based values of V_{OC}, baseline R_{int}, R_1, C_1, R_2, and C_2 remain fixed at their upper-bound second-life values in this specific scenario, while the effective internal resistance evolves through the empirical resistance-growth update. Simulations extending into the available SoH $\in$ [0.5, 0.8] interval would activate continuous SoH-dependent surface updates for the corresponding electrical parameters.

Because the empirical ageing formulation contains fitted calendar, cycling, and resistance-growth coefficients, an additional one-at-a-time sensitivity analysis was performed to assess the robustness of the long-horizon ageing outputs. The cycling-loss scale factor, resistance-growth coefficient, calendar activation energy, calendar pre-exponential factor, and SoC-dependence coefficients were perturbed around their baseline values while keeping the current profile, temperature, pack configuration, and numerical settings unchanged. The corresponding impact on final SoH and cumulative internal-resistance growth is reported in Section 3.4.

2.5. Simulation setup and automated data analysis

The entire simulation framework was implemented in MATLAB using a modular architecture that supports sequential execution of model initialization, parameter loading, dynamic simulation, and automated post-processing. Each simulation begins by initialising the model state vector, comprising the SoC and polarization voltages, and loading the relevant parameter surfaces as functions of SoC, SoH, temperature, and current direction. The simulation then iterates over a repeated 24-h duty cycle, applying the empirical ageing model (Section 2.4) to update the cell's capacity and internal resistance at the end of each simulated day.

After every cycle, voltage, current, SoC, SoH, and energy data are processed using a standardised analysis pipeline based on the DATTES framework. This ensures consistent computation of ageing and performance metrics across all model variants.

Simulation results are aggregated over a three-year equivalent operating horizon (≈1.5 million time steps), and daily performance metrics are computed, including:

- Energy throughput (Wh/day),
- Round-trip efficiency (%),
- Capacity fade and internal resistance evolution.

This automated analysis environment enables reproducible benchmarking of the four ECM topologies and supports direct comparison of their dynamic fidelity, ageing behaviour, and computational efficiency under identical operating conditions.

2.6. Numerical stability and reproducibility considerations

All ECMs were evaluated under the deterministic 24-h current profiles described in Section 3.1 and simulated over a three-year equivalent horizon, comprising approximately 1.5 million discrete time steps. The adopted time-discretisation strategy combines scalar exponential updates for the Thevenin polarization-voltage states with explicit time integration for the RC–SAFT surface–bulk redistribution states and the SoC update, using a fixed sampling period of 60 s.

This discrete-time formulation proved numerically stable across all model orders. No divergence, overflow, or undefined states (e.g., NaN values) were observed during any simulation, confirming the robustness of this formulation under prolonged execution and dynamic ageing updates.

The entire computational workflow was designed to ensure full reproducibility. The workflow is structured to generate reproducible MATLAB and CSV outputs, and simulation settings are documented to support independent verification. Each model variant relies exclusively on public datasets and analytically derived quantities, enabling independent verification and facilitating comparative studies. Moreover, the use of a standardised post-processing pipeline (DATTES) ensures consistent evaluation of energy, efficiency, and ageing metrics across different ECM topologies.

3. Results and performance analysis

3.1. Simulation setup and operating conditions

A modular simulation environment was developed to evaluate the dynamic and ageing behaviour of a 64s29p $LiFePO_4$ battery pack under controlled scenario-based operating conditions. The main cell-level parameters are summarised in Table II.

All simulations were performed at a fixed ambient temperature of 25 °C, using a one-minute sampling resolution and a repeatable 24-h current profile shown in Fig. 4, designed to represent a full charge–discharge cycle with controlled rest, discharge, and recharge phases.

The 24-h current profile was designed as a controlled benchmark rather than as a direct reproduction of a specific measured EV, hybrid-storage, or grid-service duty cycle. Its timing illustrates a daily operating schedule comprising overnight charging from 23:00 to 07:00, a dominant morning discharge from 07:00 to 09:00, a shorter midday discharge from 12:00 to 13:00, and extended low-current rest periods that represent standby and balancing operations. These time intervals were selected to provide, within one repeatable cycle, both sustained charge/discharge operation and clearly separated relaxation intervals for comparing ECM dynamics.

Smooth half-sinusoidal current segments were used instead of ideal step changes to generate well-defined but numerically smooth transitions and to excite voltage-drop and relaxation dynamics over different time scales. Under the nominal 60-Ah, 90%-DoD condition, the morning discharge is scaled so that, together with the 5-A peak midday pulse, the total nominal discharged charge is approximately 54 Ah. This results in a morning peak current of approximately 40 A. The eight-hour nighttime charging segment has a peak magnitude of approximately 11 A and restores an equivalent effective charge after accounting for the assumed charge-side coulombic efficiency of 0.95. These current magnitudes remain below the continuous and peak limits reported in Table II. The detailed definitions of the operating intervals are reported in Table III.

The resulting profile provides approximately balanced daily charge throughput under nominal conditions, thereby limiting artificial SoC drift. During the long-horizon simulation, however, SoC is not externally reset at the end of each day; it evolves dynamically through Coulomb counting using the ageing-updated capacity (C_n). The profile is repeated 1095 times, corresponding to a three-year equivalent operating horizon. After each daily cycle, the ageing laws in Eqs. (11)–(12) update the available capacity and effective internal resistance.

All four ECM configurations (RC–SAFT, Th1, Th2, and Th3) were simulated in parallel using identical current and temperature inputs. Voltage, current, SoC, SoH, and resistance trajectories were post-processed through the DATTES analysis framework to extract daily performance metrics such as energy throughput (Wh/day), round-trip efficiency (%), SoH, and internal-resistance variation (ΔR_{int}).

These daily aggregates feed back into the ageing model to compute degradation increments for the following cycle. The complete workflow is shown in Fig. 5.

Table II
Module technical data (datasheet values).

Parameter	Value
Chemistry	$LiFePO_4$ (LFP)
Nominal capacity	60 Ah
Nominal voltage	204.8 V
Operating voltage range	172.8–233.6 V
Nominal energy	12.3 kWh
Usable energy (90% DoD)	11.7 kWh
Recommended continuous current	30–60 A
Peak current (1 s)	70 A
Nominal temperature	25 °C
Guaranteed cycles	≥ 2000 (0.5C, 70% EoL (End of Life))
Weight	≈ 175 kg

Simulation outputs are cumulatively stored in dattes_output.mat, including all signal traces, figures, and performance summaries. This dataset forms the basis for the comparative analysis presented in the Sections 3.2–3.6.

3.2. Voltage dynamics and transient behaviour

The terminal-voltage dynamics of the ECM configurations were compared over the final 24-h cycle

of the simulation horizon. Fig. 6 presents the voltage trajectories produced by the RC-SAFT, Th1, Th2, and Th3 models on day 1095 under identical current and temperature inputs.

The “final simulated day” corresponds to the last day of the three-year equivalent simulation horizon,

after the maximum cumulative capacity fade and internal-resistance growth reached in the investigated

scenario have been applied. This day was selected to assess the models under the most aged condition

considered in the benchmark and to emphasise end-of-horizon differences in voltage drop, recovery, and relaxation behaviour. The comparison should therefore be interpreted as an end-of-horizon internal-

reference assessment, rather than as a fresh-cell or arbitrarily selected representative-day result.

Each model uses a discrete-time formulation to update its internal states, namely, the SoC and polarization voltages, according to the dynamics described in Section 2.2. A fixed one-minute timestep was applied across all simulations, ensuring comparability in temporal resolution and numerical integration.

The RC–SAFT model captures the dominant voltage trends but exhibits a systematic underestimation during high-power transients and post-discharge relaxation. This limitation arises from its reduced capacity to model diffusion-related polarization with sufficient time-scale separation. The first-order Thevenin model (Th1), which introduces a single RC branch for voltage recovery, improves transient tracking but still shows delayed settling and minor overshoots, especially during the transition from rest to discharge.

Relative to the internal higher-order Thevenin reference, the second-order Thevenin model (Th2) provides the closest agreement among the non-reference models over the tested operating segments. It follows both the main voltage drops and the subsequent relaxation phases more closely than RC–SAFT and Th1, indicating that the addition of a second polarization branch improves the representation of multiple voltage-relaxation time scales under the adopted current profile.

The third-order Thevenin model (Th3) introduces an additional RC branch and is used in this study as an internal higher-order numerical reference. However, as discussed in Section 2.3, the third branch is analytically derived from the available second-branch parameters rather than independently identified from dedicated third-order parameter surfaces. Therefore, its response should not be interpreted as experimentally validated ground truth. Under the adopted one-minute sampling resolution and synthetic 24-h current profile, the incremental difference between Th2 and Th3 remains limited.

These findings suggest that, within the present model-based benchmark, Th2 provides a favourable compromise between internal-reference voltage fidelity and model complexity. This conclusion is scenario-specific and should be interpreted in conjunction with the computational-performance results in Section 3.6 and the limitations discussed in Sections 3.9 and 3.10.

3.3. Energy throughput and round-trip efficiency

The energy processed by each equivalent-circuit model (ECM) was evaluated by numerically integrating the product of terminal voltage and current over each simulated day. Input (charging) and output (discharging) energies were tracked separately, and round-trip effi-

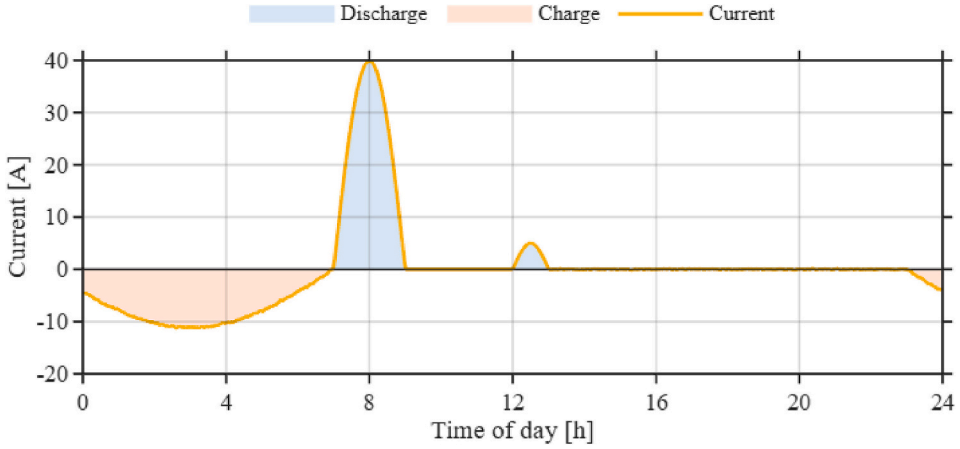

Fig. 4. Synthetic 24-h current profile used for the controlled benchmark. Positive current denotes discharge and negative current denotes charge. The profile includes a nighttime charging interval, a main morning discharge, a light midday discharge, and low-amplitude idle-current fluctuations that represent standby and balancing effects.

Table III
Synthetic 24-h Current Profile.

Operating period	Time interval	Description / formula
Morning discharge	07:00–09:00	$Ah_{\text{morning}} = C_n \cdot DoD - Ah_{\text{midday}}$
Morning rest	09:00–12:00	The module rests at nearly zero current, with small Gaussian noise ($\sigma = 0.1$ A) to emulate balancing and standby losses.
Midday discharge	12:00–13:00	$Ah_{\text{midday}} = \frac{2}{\pi} \times 5Ah$
Afternoon idle	13:00–23:00	The module rests at nearly zero current, with small Gaussian noise ($\sigma = 0.1$ A) to emulate balancing and standby losses.
Night charge	23:00–07:00	$A_{ch} = \frac{\pi}{16} \frac{C_n \cdot DoD}{\eta_{\text{charge}}}$.

ciency was computed as the ratio $\eta_{\text{day}} = E_{\text{out}}/E_{\text{in}}$, using a one-minute resolution consistent with the dynamic simulation.

Fig. 7 shows the evolution of daily energy throughput (charge + discharge) over the full three-year equivalent period. While all models follow similar trends, minor but systematic differences emerge. The RC–SAFT and Th1 models process slightly more energy than Th2 and Th3, especially during the early ageing phase (days 0–400), when increased resistance begins to affect charge acceptance and discharge efficiency.

The total energy processed over the three-year horizon is summarised in Fig. 8, confirming the order RC–SAFT > *Th*1 > *Th*2 > *Th*3. Since this quantity is computed as the sum of cumulative charge and discharge energies, the values are approximately twice the total discharged energies reported in Table IV. The total processed energy ranges from about 24.81 MWh for Th3 to about 25.09 MWh for RC–SAFT. The corresponding total discharged energy ranges from 11.69 MWh for Th3 to 12.06 MWh for RC–SAFT, as reported in Table IV. These small discrepancies reflect differences in transient overpotentials and internal losses under the same ageing law and final SoH.

Table IV reports the main energy and ageing metrics for all models under nominal conditions (25 °C, approximately 90% daily depth of discharge).

Average round-trip efficiency shows a similar trend: RC–SAFT and Th1 achieve higher efficiency (approximately 91.5–92.5%) than Th2 and Th3 (approximately 89–90%). This apparent inversion, where simpler models appear more efficient, is attributable to their reduced ability to resolve long-tail voltage relaxation, which would contribute to dissipation but is only partly represented in lower-order topologies.

These results suggest that lower-order models may be adequate for aggregate energy accounting, whereas higher-order ECMs become more relevant when detailed voltage dynamics or control-layer accuracy is required.

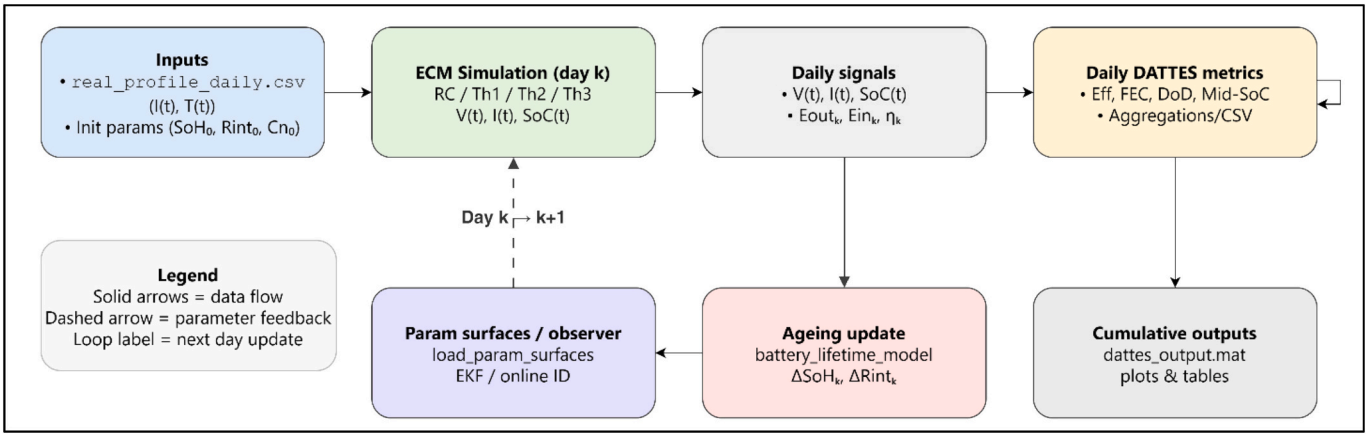

Fig. 5. Simulation and data pipeline. Each day:
Inputs → ECM simulation → Post-processing (V, I, SoC) → DATTES metrics → Ageing update → New parameters → Next day.

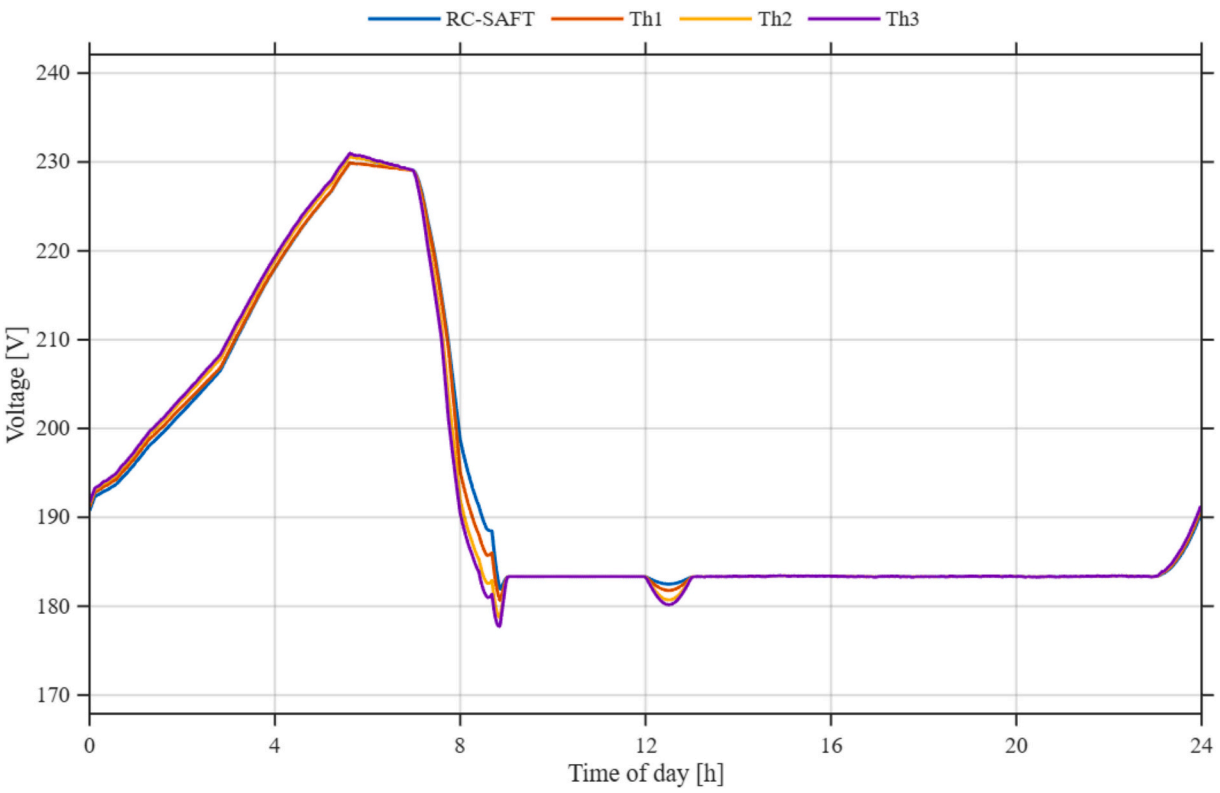

Fig. 6. Overlay of simulated terminal-voltage trajectories for the tested ECM configurations on the final simulated day, corresponding to day 1095 of the three-year equivalent horizon after cumulative ageing updates. All models are evaluated under the same 24-h current profile and fixed-temperature conditions. The comparison highlights end-of-horizon differences in voltage drop and relaxation behaviour among the RC-SAFT, Th1, Th2, and Th3 models.

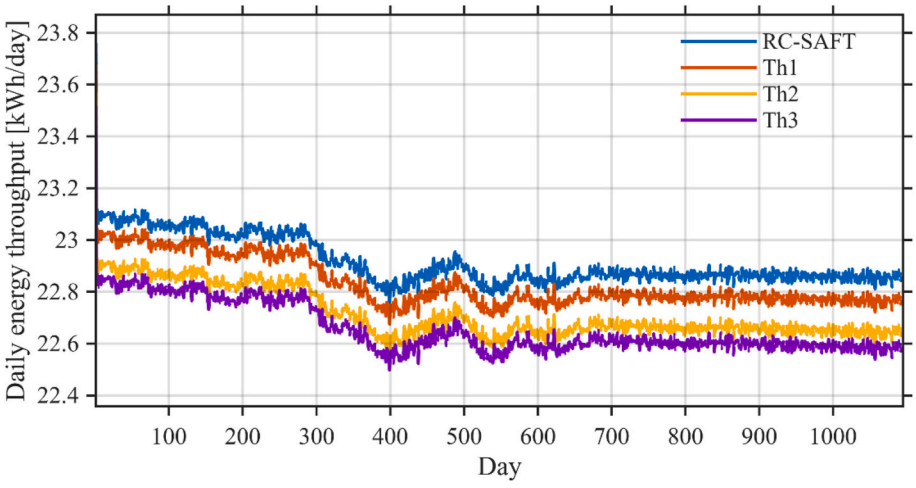

Fig. 7. Scenario-specific daily energy throughput over the three-year equivalent simulation horizon for the tested ECM configurations. Daily throughput is computed as the sum of charge and discharge energy for each repeated 24-h cycle. The small differences among models reflect their different representations of transient overpotentials and voltage-relaxation losses under the same current profile and ageing assumptions.

To verify that the RC–SAFT energy indicators were not biased by the selected capacity-splitting factor, an additional robustness check was performed by varying α from 0.10 to 0.50. The results confirmed that the long-horizon energy metrics are practically insensitive to this parameter. With respect to the baseline value $\alpha = 0.20$, the average round-trip efficiency varied by only about 0.0005 percentage points, while the total discharged energy changed by less than 0.012%. The main influence of α was observed in the voltage redistribution dynamics: $\alpha = 0.10$ increased the RMSE relative to the internal Th2 reference, whereas values $\alpha \geq 0.20$ produced an almost flat RMSE plateau. This confirms that the efficiency and energy-throughput conclusions are robust with respect to the RC–SAFT capacitance split.

3.4. Ageing behaviour and state of health (SoH) evolution

Long-term battery degradation was simulated by applying the empirical ageing model described in Section 2.4 at the end of each daily cycle. Both calendar and cycling contributions were updated based on the operating temperature, SoC trajectory, and daily depth of discharge, resulting in a progressive loss of capacity (SoH) and increase in internal

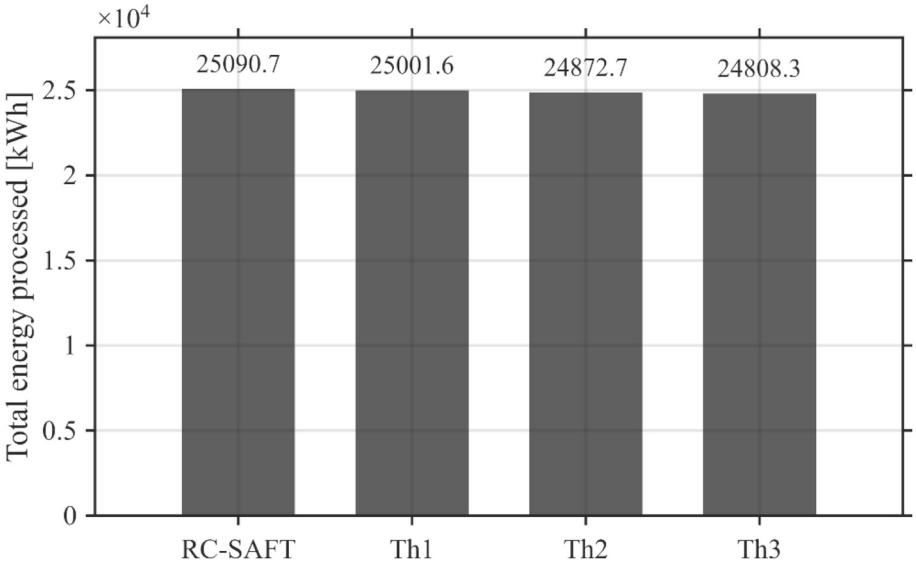

Fig. 8. Scenario-specific total energy processed over the three-year equivalent simulation horizon for each ECM configuration. Total processed energy is computed as the sum of the cumulative charge and discharge energies over all repeated 24-h cycles. The small differences among models arise from their different representations of transient overpotentials and voltage-relaxation losses under the same current profile and ageing assumptions.

Table IV
Energy and ageing indicators (three-year equivalent operation, 25 °C, ~90% DoD/day).

Model	Avg. efficiency (%)	Final SoH (%)	ΔR_{int} (%)	Total discharged energy (MWh)
RC–SAFT	92.51	83.47	+19.83	12.057
Th1	91.53	83.47	+19.83	11.948
Th2	89.90	83.47	+19.83	11.775
Th3	89.09	83.47	+19.83	11.689

resistance (ΔR_{int}).

As shown in Fig. 9 and Fig. 10, all ECM configurations exhibit identical ageing trajectories, with SoH declining smoothly from 100% to ≈83.47% over the three-year equivalent horizon, and internal resistance increasing by +19.83%. These identical trajectories reflect the modular structure of the implemented ageing update. In the present framework, the ageing law is driven by common daily stress indicators and empirical coefficients, rather than by ECM-specific polarization states, transient overpotential histories, or local electrochemical variables. Therefore, the identical SoH and resistance-growth trajectories should be interpreted as a consequence of the adopted ageing-coupling strategy, not as a general proof that ECM order has no influence on degradation in real batteries.

3.4.1. *Sensitivity of ageing outputs to empirical coefficients*

To assess whether the ageing outputs depend strongly on the selected empirical coefficients, a one-at-a-time sensitivity analysis was performed on the main ageing-law parameters. The cycling-loss scale factor, resistance-growth coefficient, calendar activation energy, calendar pre-exponential factor, and SoC-dependence coefficients were perturbed around their baseline values while keeping the current profile, temperature, pack configuration, and numerical settings unchanged. The stand-alone ageing-sensitivity calculation gave a baseline final SoH of 83.56% and a cumulative internal-resistance increase of 19.73%, which is consistent with the full ECM simulations. Table V reports the resulting parameter-dependent ranges and the maximum deviations

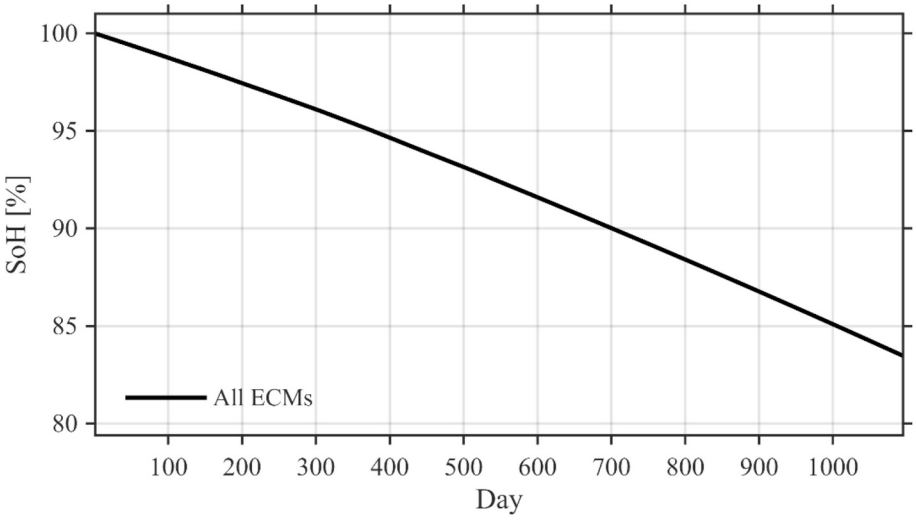

Fig. 9. State-of-health trajectory over the three-year equivalent simulation horizon. The single curve represents all tested ECM configurations, which overlap because the empirical ageing update is driven by common daily stress indicators rather than by ECM-specific polarization states or transient overpotential histories.

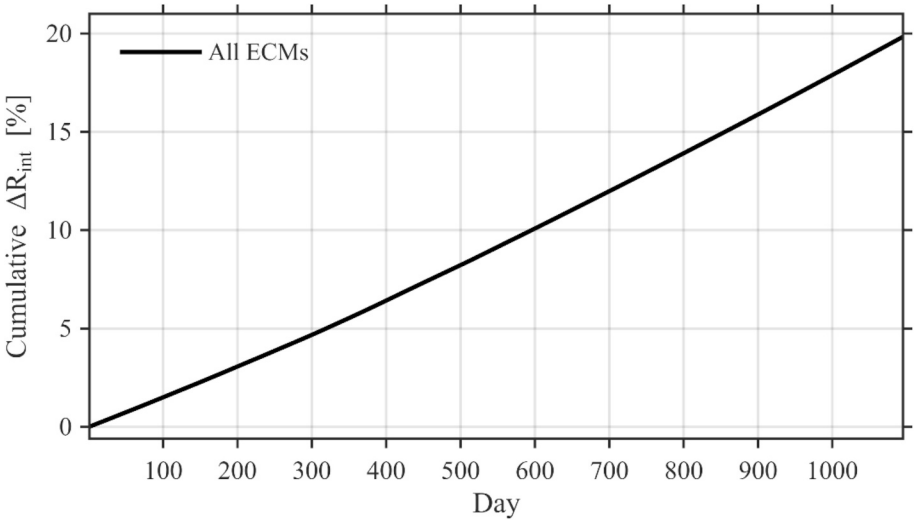

Fig. 10. Cumulative internal-resistance growth over the three-year equivalent simulation horizon. The trajectories overlap for all ECM configurations because the empirical ageing update is driven by common daily stress indicators, rather than by ECM-specific polarization states or transient overpotential histories.

from this sensitivity baseline. The baseline values in Table V are obtained from the stand-alone ageing-sensitivity routine and therefore differ slightly from the full ECM simulation values reported in Table IV.

The sensitivity results show that the final SoH is mainly governed by the cycling-loss scale factor. This parameter modifies the accumulated cycling-related capacity loss and therefore directly affects the final capacity fade. By contrast, the resistance-growth factor k_{rint} does not affect final SoH, but it directly scales the cumulative internal-resistance increase. As expected, ΔR_{int} is therefore sensitive both to the cycling-loss scale and to k_{rint}. The calendar-related coefficients have a smaller influence under the adopted fixed-temperature, daily-repeated cycling scenario, whereas the SoC-dependence coefficients exhibit negligible variation.

These findings clarify two distinct aspects of the ageing analysis. First, the relative comparison among ECMs remains unchanged because the same ageing law is consistently applied across all model configurations. Second, the absolute degradation values remain conditional on the selected empirical ageing coefficients. Consequently, the reported final SoH and resistance-growth values should be interpreted as scenario-specific outputs of the adopted empirical ageing model, rather than as experimentally validated predictions for a specific real battery pack.

3.5. Internal resistance growth and efficiency degradation

Although all simulations were conducted at a fixed temperature of 25 °C, the gradual increase in internal resistance observed across all ECMs, reaching +19.83% after three years, demonstrates the cumulative impact of ageing-induced ohmic losses. This resistance growth reduces the effective voltage during discharge and increases losses during charge, thus directly degrading the round-trip energy efficiency.

Fig. 11 illustrates the monthly average correlation between round-trip efficiency (η) and internal resistance increase (ΔR_{int}) for each ECM configuration. A clear, nearly linear trend is observed: as ΔR_{int} increases, efficiency declines systematically. Under the adopted fixed-temperature scenario, the fitted monthly trend corresponds to an apparent efficiency decrease of approximately 0.09 pp. per 1% increase in ΔR_{int}.

While this correlation is captured under isothermal conditions, it is expected to intensify under realistic, non-isothermal operation. In such cases, the ageing rate, particularly calendar ageing, would follow an Arrhenius-type exponential dependence on temperature, as per Eq. (8). Consequently, temperature fluctuations would accelerate both capacity fade and resistance growth, further penalising efficiency.

The modular structure of the proposed framework enables seamless integration of temperature-dependent ageing models, paving the way for fully coupled thermal–electrical simulations. This extension would be useful for future digital-twin-oriented studies tasked with real-time lifetime prediction under variable ambient and internal thermal conditions.

3.6. Computational performance

The computational cost of each ECM configuration was assessed using two complementary timing benchmarks, with all runtimes normalised to the RC–SAFT baseline. The primary and most repeatable metric is a per-step micro-benchmark, in which each model advances a

Table V
One-at-a-time sensitivity of the final ageing indicators to the empirical ageing-law parameters. Each parameter is perturbed individually about its baseline value while all other inputs, parameter surfaces, and numerical settings are kept fixed. Deviations are reported with respect to the sensitivity baseline SoH_{final} = 83.56% and ΔR_{int} = +19.73% (pp = percentage points).

Perturbed parameter	Perturbation range	Final *SoH* range [%]	ΔR_{int} range [%]	Max $\lvert\Delta SoH_{final}\rvert$ [pp]	Max $\lvert\Delta R_{int}\rvert$ [pp]	Main effect
Cycling-loss magnitude $k_{cyc,scale}$	±20%	79.84–87.10	15.48–24.19	3.72	4.46	Dominant effect on capacity fade
Resistance-growth factor k_{rint}	±20%	83.56 (unchanged)	15.79–23.68	0.00	3.95	Direct effect on resistance growth
Calendar activation energy E_a	±10%	82.92–83.79	19.45–20.49	0.64	0.76	Moderate calendar sensitivity
Calendar pre-exponential factor A_{cal}	±20%	83.47–83.62	19.66–19.84	0.09	0.11	Weak effect
SoC coefficient *a*	±20%	83.53–83.58	19.70–19.76	0.03	0.03	Negligible effect
SoC coefficient *b*	±20%	83.51–83.61	19.67–19.79	0.05	0.06	Negligible effect

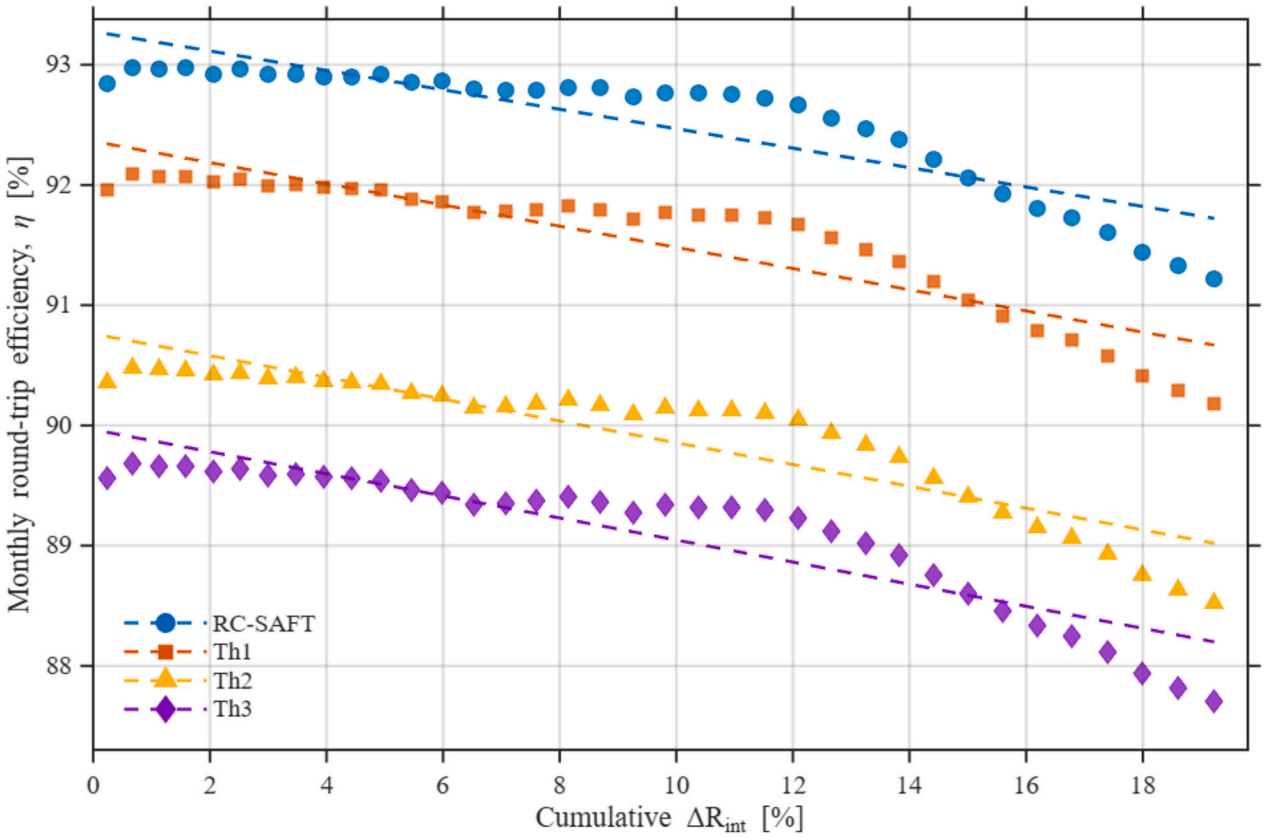

Fig. 11. Monthly correlation between round-trip efficiency and cumulative internal-resistance growth across the tested ECM configurations over the three-year equivalent simulation horizon. Symbols indicate monthly averaged values and dashed lines indicate linear regression fits. The trend shows the progressive efficiency reduction associated with ageing-induced resistance growth under the fixed-temperature repeated-cycle scenario.

fixed-length current sequence using fixed parameters and no parameter-surface interpolation. This benchmark isolates the cost of the electrical state-update equations. As an implementation-level cross-check, a 100-day simulation workflow benchmark was also performed, with SoH-indexed parameter interpolation and the daily ageing update included inside the timed loop.

The two computational benchmarks serve different interpretive purposes. The per-step micro-benchmark is used as the primary computational index for the fidelity–runtime comparison because it isolates the electrical state-update cost of each ECM under identical input length and fixed parameter conditions. This makes it the most direct measure of the electrical state-update burden associated with each ECM implementation. By contrast, the 100-day workflow benchmark includes parameter interpolation, daily ageing updates, data handling, and loop-management overheads. It is therefore useful as an implementation-level robustness check, but it mixes ECM-specific costs with common workflow operations. For this reason, Fig. 14 uses the per-step runtime index, while the 100-day workflow benchmark is reported to demonstrate that the same qualitative runtime ordering is preserved when the full simulation workflow is considered. Each benchmark was repeated seven times after one warm-up run. Table VI reports the mean relative runtime and the run-to-run spread, computed as the standard deviation normalised to the mean RC–SAFT runtime of the corresponding benchmark. All measurements were obtained using MATLAB R2025b on a 64-bit Windows platform equipped with an Intel(R) Core (TM) i7-6560U CPU @ 2.20 GHz and 16 GB installed RAM. MATLAB was configured to use up to 2 computational threads during the benchmark.

Table VI summarises the resulting computational indices. In the per-step benchmark, the mean computational cost increases monotonically within the Thevenin family, following the expected order Th1 < Th2 < Th3. This trend is consistent with the addition of one polarization state at each model order. The corresponding relative per-step runtimes are 0.48, 0.50, and 0.54 for Th1, Th2, and Th3, respectively. The RC–SAFT model is the most expensive configuration in this benchmark, with a relative runtime of 1.00.

This result indicates that topological simplicity does not necessarily imply a cheaper numerical update. In the present MATLAB implementation, the RC–SAFT update recomputes the equivalent electro-

Table VI
Relative computational cost and static storage index of the equivalent-circuit models, normalised to the RC–SAFT baseline (= 1.00). The per-step runtime is the primary repeatable index and isolates the electrical state-update equations using fixed parameters and no parameter-surface interpolation. The 100-day simulation-workflow runtime includes SoH-indexed parameter interpolation and the daily ageing update inside the timed loop. Runtime values are means over seven repeats; the spread is the standard deviation normalised to the mean RC–SAFT runtime of the corresponding benchmark.

Model	Per-step runtime, mean rel.	Per-step spread [% baseline]	Full-workflow runtime, mean rel.	Full-workflow spread [% baseline]	Static storage index	State dimension
RC–SAFT	1.00	29.3	1.00	27.5	1.00	3
Th1	0.48	13.1	0.61	6.9	0.89	2
Th2	0.50	16.2	0.66	13.3	1.22	3
Th3	0.54	9.8	0.75	29.7	1.33	4

chemical capacitance terms, the clipped diffusion-like time constant, the exchange resistance (R_e), and the surface/bulk capacitance split, and then advances the two coupled charge-redistribution states. By contrast, the Thevenin models use compact scalar exponential updates for the polarization voltages. Therefore, the larger per-step arithmetic associated with the RC–SAFT formulation outweighs its lower conceptual order.

The 100-day simulation workflow benchmark preserves the same mean ordering. The RC–SAFT baseline remains the most expensive configuration, while the Thevenin models show increasing relative cost with order: 0.61 for Th1, 0.66 for Th2, and 0.75 for Th3. Since parameter interpolation and daily ageing updates are common workflow operations, they introduce shared overheads that partially compress the relative differences observed in the isolated per-step benchmark. Nevertheless, the same qualitative ordering is maintained.

The static storage requirement is small for all configurations and is not a limiting factor in the present simulations. As expected, the state dimension increases from two states in Th1 to four states in Th3. The static storage index reported in Table VI is a coarse implementation-level proxy based on the number of state variables and parameters held at each step; it is not a measured MATLAB memory profile.

These computational indices should be interpreted as indicative, implementation- and platform-dependent software benchmark results rather than intrinsic properties of the model equations. They depend on the specific MATLAB implementation, coding style, scalar/vectorised operations, and hardware configuration, and could change under different programming languages or processor architectures. This is also reflected in the run-to-run spread reported in Table VI, which is appreciable for the RC–SAFT baseline and for the full-workflow Th3 case. Within these limits, the benchmark supports the scenario-specific conclusion that the second-order Thevenin model provides a favourable internal-reference voltage-fidelity–cost compromise: its per-step cost is close to that of Th1 and substantially lower than that of the RC–SAFT formulation, while its voltage fidelity is much closer to the internal higher-order Thevenin reference.

3.7. Internal reference fidelity and transient accuracy assessment

To quantify the internal-reference fidelity of each ECM configuration, we evaluated the simulated terminal voltage against the third-order Thevenin model (Th_3), which is used as an internal higher-order numerical reference. The analysis focuses on the final day of simulation, where cumulative ageing effects are most pronounced.

The following fidelity metrics were computed:

- **RMSE** (Root Mean Square Error): average magnitude of voltage deviation from the reference (Th3).
- **NRMSE** (Normalised RMSE): RMSE expressed as a percentage of the nominal voltage (204.8 V), to enable scale-independent comparisons.
- **ρ (Pearson Correlation Coefficient)**: measures linear correlation between model and reference voltages (ρ = 1 indicates perfect correlation).
- **TVE** (Total Vector Error): a composite metric (%) that accounts for both amplitude and phase mismatches.

These metrics were computed over the full 24-h voltage waveform of the final simulated day. Results are shown in Table VII.

In addition to global metrics, Fig. 12 presents a zoomed comparison of two representative transient segments:

1. **Post-discharge voltage recovery** (≈ 09:00), where surface–bulk redistribution dominates;
2. **End-of-charge relaxation** (≈ 07:00), highlighting short-time polarization effects.

Table VII
Dynamic fidelity metrics for each ECM compared to Th3 on the final day.

Model	RMSE [V]	NRMSE [%]	ρ	TVE [%]
RC–SAFT	1.886	0.962	0.9905	0.452
Th1	1.353	0.690	0.9952	0.327
Th2	0.451	0.230	0.9995	0.109

The RC–SAFT model exhibits underdamped behaviour and residual offset, while Th1 resolves only the dominant polarization mode. Th2, in contrast, closely matches the Th3 reference in both transients, confirming its ability to resolve multiple time constants with minimal computational overhead.

These results support the use of Th2 as a favourable internal-reference fidelity–complexity compromise within the present benchmark.

3.8. Reproducibility and data integrity

Ensuring reproducibility and transparency was a primary design objective throughout the development of the proposed simulation framework. A dedicated post-processing environment, DATTES (Data analysis tools for tests on energy storage), automatically computes, organises, and exports key ageing and performance indicators for each simulated day.

For every 24-h cycle, the framework generates structured records that map raw time-series data (current, voltage, and temperature) to high-level quantities such as SoC, SoH, charge/discharge energies, round-trip efficiency, and internal resistance growth. These metrics are computed through a consistent and standardised pipeline, which includes time alignment, noise filtering, energy balance estimation, and resistance tracking based on empirical ageing laws.

All results are saved both as structured MATLAB objects and as interoperable CSV exports, such as daily_summary.csv, energy_metrics.csv, rint_growth.csv, and soh_trajectory.csv, supporting traceability, independent inspection, reproducibility checks, and integration with third-party analysis tools.

Fig. 13 illustrates this reproducibility-oriented workflow, showing how raw electrical inputs are transformed into concise daily summaries that enable robust comparison across models and scenarios.

3.9. Discussion: model-selection implications and scope of the benchmark

The comparative results highlight that the relevance of ECM order depends strongly on the performance indicator considered. Energy-related quantities, such as daily energy throughput, total discharged energy, and average round-trip efficiency, vary only moderately across the tested ECMs. These differences arise from the way each model represents transient overpotentials and voltage relaxation, but they remain limited compared with the overall long-horizon energy processed by the pack. The robustness check on the RC–SAFT capacity-splitting factor further confirms that the RC–SAFT energy indicators are not sensitive to the selected value of α, since round-trip efficiency and total discharged energy remained practically unchanged over the investigated range.

By contrast, ECM order has a more visible impact on voltage dynamics. To summarise this behaviour in a BMS-relevant way, rank-based waveform similarity indicators were computed by comparing each model voltage trajectory with the internal Th3 reference on the final simulated day. The Spearman coefficient ρ_S measures the monotonic agreement between the ranked voltage sequences, thereby reducing sensitivity to small absolute voltage offsets. The weighted Spearman coefficient ρ_w is computed as a weighted rank-correlation indicator, with weights proportional to the absolute current magnitude $|I|$, so that high-current charge and discharge intervals contribute more strongly than idle periods. Similarly, Kendall's τ_k measures pairwise concordance between the model and reference voltage sequences, while the weighted

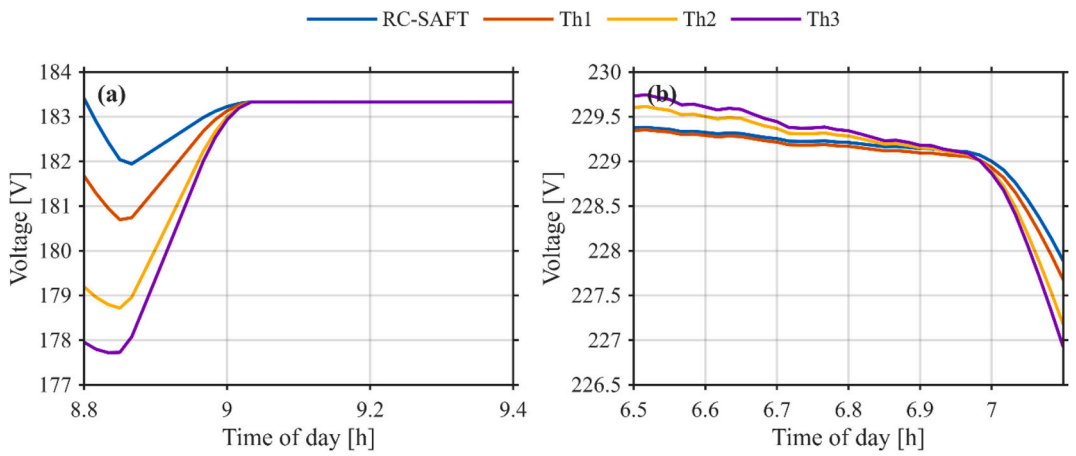

Fig. 12. Zoomed comparison of terminal-voltage transients for the tested ECMs on the final simulated day: (a) post-discharge relaxation around 09:00; (b) end-of-charge transition around 07:00. The comparison highlights the different voltage-recovery and relaxation behaviour of the RC-SAFT, Th1, Th2, and Th3 models under the same current profile.

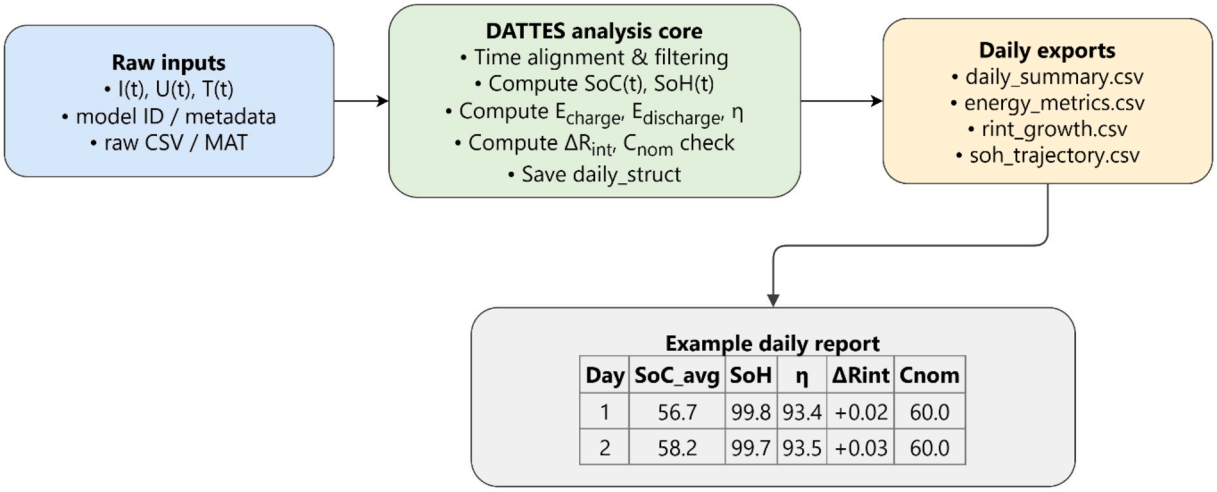

Fig. 13. DATTES data-processing pipeline from raw I–V–T inputs to structured daily indicators.
The framework generates consistent daily reports used for post-analysis and reproducibility validation.
A sample report is shown at the bottom.

Kendall coefficient τ_w applies the same current-based weighting concept to emphasise dynamically relevant operating segments [33].

Table VIII reports these internal-reference fidelity indicators together with the relative per-step runtime taken from the computational benchmark in Table VI. The results show a progressive improvement in voltage-fidelity indicators from RC–SAFT to Th1 and Th2, with Th3 serving as the internal higher-order numerical reference. In particular, Th2 achieves a weighted Spearman coefficient of $\rho_w = 0.991$, indicating that it preserves the current-weighted voltage-ranking structure of the internal Th_3 reference, while retaining a relative per-step runtime of 0.50 with respect to the RC–SAFT baseline. This indicates that, within the adopted benchmark, adding a second polarization branch substantially improves the representation of transient voltage recovery and relaxation, whereas the additional gain associated with the third branch is comparatively small under the tested one-minute sampling resolution and current profile.

The fidelity–runtime landscape is summarised in Fig. 14. The figure uses the per-step runtime benchmark as the computational index, consistently with Table VI and Table VIII. In this representation, RC–SAFT lies outside the Pareto frontier because it combines lower internal-reference voltage fidelity with a higher per-step cost than the tested Thevenin configurations in the present MATLAB implementation.

Table VIII
Internal-reference fidelity and per-step runtime metrics for the ECM configurations. Runtime values are taken from the per-step micro-benchmark in Table VI and are normalised to the RC–SAFT baseline. Th_3 is used as the internal higher-order numerical reference for the fidelity metrics.

Model	ρ_S	ρ_w	τ_k	τ_w	Relative per-step runtime	Interpretation
RC–SAFT	0.980	0.865	0.933	0.903	1.00	Interpretable surface–bulk model, lower internal-reference fidelity
Th1	0.992	0.945	0.959	0.935	0.48	Lowest-cost Thevenin configuration, moderate fidelity
Th2	**0.999**	**0.991**	**0.987**	**0.980**	**0.50**	**Favourable fidelity–cost compromise in this benchmark**
Th3	1.000	1.000	1.000	1.000	0.54	Internal higher-order numerical reference

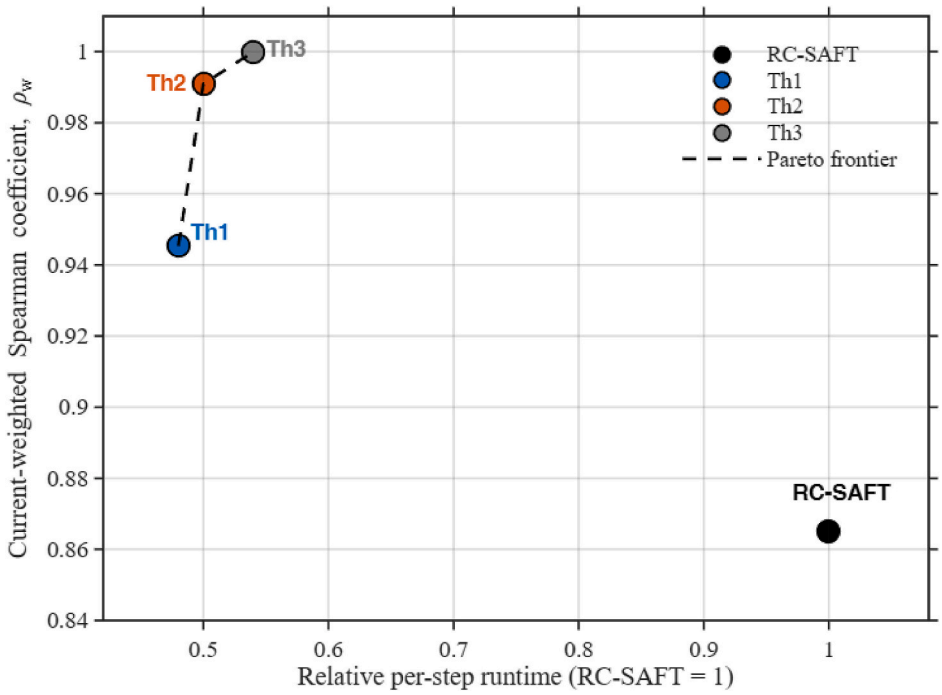

Fig. 14. Current-weighted Spearman voltage-fidelity indicator versus relative per-step runtime for the tested ECMs. The runtime axis uses the isolated per-step micro-benchmark from Table VI, since this benchmark directly reflects the electrical state-update cost of each ECM, without parameter-interpolation or daily-ageing workflow overheads. The 100-day workflow benchmark is reported separately in Table VI as an implementation-level cross-check. Runtime values are normalised to the RC–SAFT baseline, and the Pareto frontier highlights the scenario-specific fidelity–cost trade-off within the adopted MATLAB implementation.

Within the Thevenin family, runtime increases with model order, following the expected sequence Th1 < Th2 < Th3. Th1 provides the lowest per-step cost but lower voltage fidelity; Th3 provides the internal reference waveform but at the highest Thevenin cost; and Th2 lies between them, providing the most favourable scenario-specific compromise between internal-reference fidelity and per-step computational effort.

The computational results should therefore be interpreted as implementation-level indicators rather than intrinsic properties of the model equations. As discussed in Section 3.6, the per-step benchmark isolates the electrical state update, whereas the 100-day simulation-workflow benchmark includes SoH-indexed parameter interpolation and daily ageing updates. Both benchmarks preserve the same mean ordering, but their absolute relative values depend on the MATLAB implementation, coding style, vectorisation choices, and hardware configuration. The runtime values should therefore not be generalised as universal computational rankings across programming languages or embedded platforms.

The ageing results require a separate interpretation. All ECMs produce identical SoH and internal-resistance-growth trajectories because the adopted ageing module is driven by common daily stress indicators, such as calendar conditions and cycling-related quantities, rather than by ECM-specific polarization states, transient overpotential histories, or local electrochemical variables. Consequently, the identical degradation trajectories should be interpreted as a property of the implemented modular ageing-coupling strategy. They do not prove that ECM topology is generally irrelevant to ageing in real batteries. A different ageing formulation explicitly dependent on overpotential, temperature gradients, local SoC distribution, or estimator-derived internal states could lead to model-dependent degradation predictions.

From a BMS and digital-twin workflow perspective, these findings suggest a practical model-selection hierarchy within the adopted benchmark. The RC–SAFT formulation remains useful when an interpretable surface–bulk charge-redistribution structure is desired, although in the present MATLAB implementation it is not the least expensive option. Th1 is the lowest-cost Thevenin configuration and may be suitable for applications where moderate transient fidelity is sufficient. Th2 offers the most balanced result in the present study because it captures the main voltage-relaxation features while retaining a per-step cost close to that of Th1 and substantially lower than that of the RC–SAFT baseline. Th3 is useful as an internal higher-order numerical reference for offline comparison, but its third branch is not independently identified from dedicated third-order parameter surfaces and its incremental benefit is limited under the tested conditions.

These implications are intentionally scenario-specific. The benchmark was performed for a 64s29p $LiFePO_4$ pack, fixed 25 °C operation, open SoC–SoH-dependent parameter surfaces, an empirical calendar–cycling ageing law, and a repeated synthetic 24-h current profile. The conclusions therefore quantify relative behaviour within this controlled MATLAB workflow. They should not be interpreted as experimental validation of absolute voltage accuracy, efficiency, or degradation prediction for a real battery pack. Extending the workflow to measured dynamic current–voltage data, electro-thermal coupling, multi-chemistry datasets, and estimator-in-the-loop operation is necessary before drawing predictive conclusions for operational BMS or field-deployed digital twins.

3.10. *Limitations of the present benchmarking study*

This study has several limitations that must be considered when interpreting the results. First, the benchmark does not include direct experimental validation against measured dynamic current–voltage data from a real cell or pack under the same operating profile. Therefore, the voltage-fidelity metrics quantify agreement among model variants, using the third-order Thevenin model as an internal reference, and should not be interpreted as absolute accuracy with respect to real battery behaviour.

Second, the simulations are restricted to a single 64s29p $LiFePO_4$ battery pack configuration, fixed 25 °C operation, and a repeated synthetic 24-h current profile. The profile was designed for controlled

comparison and does not represent a measured EV drive cycle or grid-storage duty cycle. Thermal variation, electro-thermal coupling, multi-chemistry comparison, and heterogeneous pack behaviour are not included.

Third, the ageing law is driven by common daily stress metrics and does not explicitly use ECM-specific polarization voltages, transient overpotential histories, local SoC gradients, or internal thermal states. Consequently, the identical SoH and ΔRint trajectories observed across ECMs are a consequence of the implemented ageing-coupling strategy and should not be generalised to all ageing-aware battery models.

Fourth, the computational-performance results are specific to the implemented MATLAB workflow, hardware platform, coding style, interpolation handling, and benchmark configuration. They are useful for evaluating the present implementation but should not be treated as intrinsic model-order scalability measures.

Accordingly, the proposed framework should be interpreted as a reproducible model-based benchmarking platform for controlled ECM comparison. Experimental validation, electro-thermal ageing coupling, ECM-state-sensitive degradation modelling, multi-chemistry testing, and estimator-in-the-loop implementation are required before predictive deployment in operational BMS or battery digital-twin systems.

4. Conclusion and future work

This study presented a reproducible MATLAB-based benchmarking workflow for comparing a RC–SAFT model and first-, second-, and third-order Thevenin equivalent-circuit models at battery-pack scale under common parameterisation, operating, and ageing assumptions. The workflow combines open SoC–SoH-dependent parameter surfaces, explicit boundary handling of the available second-life SoH domain, an empirical calendar–cycling ageing update, and standardised post-processing through the DATTES toolbox.

Within the investigated 64s29p $LiFePO_4$ benchmark, fixed-temperature operation, repeated synthetic 24-h current profile, and MATLAB implementation, the results show that ECM order has a stronger influence on voltage dynamics than on long-horizon energy indicators. The second-order Thevenin model provided the most favourable compromise between internal-reference fidelity and cost among the tested configurations. It approached the voltage-ranking behaviour of the internal higher-order Thevenin reference while retaining a per-step runtime close to that of the first-order Thevenin model and substantially below the RC–SAFT baseline in the adopted implementation. The third-order Thevenin model was useful as an internal higher-order numerical reference, but its additional branch was not independently identified from dedicated third-order parameter surfaces and provided limited incremental benefit under the tested conditions.

The ageing results must be interpreted within the adopted modular coupling strategy. All ECM configurations produced identical SoH and internal-resistance-growth trajectories because the empirical ageing law was driven by common daily stress indicators and empirical coefficients, rather than by ECM-specific polarization states, transient overpotential histories, or local electrochemical variables. Therefore, these results do not demonstrate that ECM topology is generally irrelevant to degradation in real batteries. They show that, within the implemented framework, ageing stress can be held constant while the dynamic and computational behaviour of different ECM topologies is compared. The ageing-parameter sensitivity analysis further confirmed that the absolute degradation values are conditional on the selected empirical coefficients, with the cycling-loss scale and resistance-growth factor having the largest influence on the final SoH and cumulative resistance increase.

The proposed workflow is therefore best interpreted as a transparent and reproducible model-based benchmarking platform, rather than as an experimentally validated predictive battery digital twin. Its main value lies in enabling controlled comparison of ECM family and order under common assumptions, with traceable post-processing and scenario-specific performance indicators. Future work should extend the framework through validation against measured dynamic current–voltage data, electro-thermal coupling, ageing laws that depend explicitly on internal ECM states or local electrochemical variables, multi-chemistry and heterogeneous-pack testing, and estimator-in-the-loop implementation. These extensions are necessary before the workflow can be used for predictive deployment in operational BMS or field-level battery digital-twin applications.

CRediT authorship contribution statement

Sara Carcangiu: Writing – review & editing, Writing – original draft, Software, Methodology, Formal analysis, Data curation, Conceptualization. **Santhosh Paramasivam:** Writing – review & editing, Writing – original draft, Visualization, Methodology, Formal analysis, Data curation, Conceptualization. **Amit Kumar:** Writing – review & editing, Validation, Supervision, Project administration, Methodology, Data curation, Conceptualization. **Fabrizio Pilo:** Writing – review & editing, Supervision, Resources, Methodology, Funding acquisition, Formal analysis, Conceptualization. **Gianluca Gatto:** Writing – review & editing, Supervision, Resources, Methodology, Funding acquisition, Formal analysis, Conceptualization.

Declaration of Generative AI and AI-assisted technologies in the writing process

Grammarly - AI-assisted tool was used solely to improve language quality, structural clarity, and overall readability of the manuscript. No AI tools were used for data analysis, model development, simulation, result generation, or scientific interpretation. The authors take full responsibility for the technical content, analysis, and conclusions presented in this work.

Declaration of competing interest

The authors declare that they have no known competing financial interests or personal relationships that could have appeared to influence the work reported in this paper.

Acknowledgements

This work was partially carried out under the National Recovery and Resilience Plan (PNRR), of Italian Ministry of University and Research under the Next-Generation EU Programme, Network 4 Energy Sustainable Transition – NEST project code: PE0000021, and Ecosystem of Innovation for Next Generation Sardinia – *e.INS* project code ECS0000038.

Data availability

Data will be made available on request.

References

[1] B. Zheng, Z. Deng, Z. Luo, S. Mao, M. Ouyang, X. Han, H. Wang, Y. Li, Y. Sun, D. Wang, Y. Yuan, L. He, Z. Yang, Y. Zhu, A comprehensive review of lithium-ion battery modelling research and prospects: in-depth analysis of current research and future directions, Appl. Energy 401 (2025) 126688, https://doi.org/10.1016/j.apenergy.2025.126688.

[2] S.S. Madani, Y. Shabeer, F. Allard, M. Fowler, C. Ziebert, Z. Wang, S. Panchal, H. Chaoui, S. Mekhilef, S.X. Dou, K. See, K. Khalilpour, A comprehensive review on lithium-ion battery lifetime prediction and aging mechanism analysis, Batteries 11 (2025) 127, https://doi.org/10.3390/batteries11040127.

[3] I. Gwayi, S.P. Ayeng'o, C.Z.M. Kimambo, A review of Lithium-ion battery empirical and semi-empirical aging models for off-grid renewable energy systems application, Eng. Rep. 7 (2025) e70169, https://doi.org/10.1002/eng2.70169.

[4] M. Chen, G.A. Rincon-Mora, Accurate electrical battery model capable of predicting runtime and I-V performance, IEEE Trans. Energy Convers. 21 (2006) 504–511, https://doi.org/10.1109/TEC.2006.874229.
[5] O. Tremblay, L.-A. Dessaint, A.-I. Dekkiche, A generic battery model for the dynamic simulation of hybrid electric vehicles, in: 2007 IEEE Vehicle Power and Propulsion Conference, IEEE, Arlington, TX, USA, 2007, pp. 284–289, https://doi.org/10.1109/VPPC.2007.4544139.
[6] H. He, R. Xiong, J. Fan, Evaluation of lithium-ion battery equivalent circuit models for state of charge estimation by an experimental approach, Energies 4 (2011) 582–598, https://doi.org/10.3390/en4040582.
[7] X. Hu, S. Li, H. Peng, A comparative study of equivalent circuit models for Li-ion batteries, J. Power Sources 198 (2012) 359–367, https://doi.org/10.1016/j.jpowsour.2011.10.013.
[8] M.A.A. Mohamed, T.F. Yu, G. Ramsden, J. Marco, T. Grandjean, Advancements in parameter estimation techniques for 1RC and 2RC equivalent circuit models of lithium-ion batteries: a comprehensive review, J. Energy Storage 113 (2025) 115581, https://doi.org/10.1016/j.est.2025.115581.
[9] J. Rivera-Barrera, N. Muñoz-Galeano, H. Sarmiento-Maldonado, SoC estimation for lithium-ion batteries: review and future challenges, Electronics 6 (2017) 102, https://doi.org/10.3390/electronics6040102.
[10] L. Yao, S. Xu, A. Tang, F. Zhou, J. Hou, Y. Xiao, Z. Fu, A review of Lithium-ion battery state of health estimation and prediction methods, WEVJ 12 (2021) 113, https://doi.org/10.3390/wevj12030113.
[11] M.A. Hannan, M.S.H. Lipu, A. Hussain, A. Mohamed, A review of lithium-ion battery state of charge estimation and management system in electric vehicle applications: challenges and recommendations, Renew. Sust. Energ. Rev. 78 (2017) 834–854, https://doi.org/10.1016/j.rser.2017.05.001.
[12] X. Liu, Y. Gao, K. Marma, Y. Miao, L. Liu, Advances in the study of techniques to determine the Lithium-ion battery's state of charge, Energies 17 (2024) 1643, https://doi.org/10.3390/en17071643.
[13] W. Waag, C. Fleischer, D.U. Sauer, Critical review of the methods for monitoring of lithium-ion batteries in electric and hybrid vehicles, J. Power Sources 258 (2014) 321–339, https://doi.org/10.1016/j.jpowsour.2014.02.064.
[14] M. Berecibar, I. Gandiaga, I. Villarreal, N. Omar, J. Van Mierlo, P. Van Den Bossche, Critical review of state of health estimation methods of Li-ion batteries for real applications, Renew. Sust. Energ. Rev. 56 (2016) 572–587, https://doi.org/10.1016/j.rser.2015.11.042.
[15] J. Klee Barillas, J. Li, C. Günther, M.A. Danzer, A comparative study and validation of state estimation algorithms for Li-ion batteries in battery management systems, Appl. Energy 155 (2015) 455–462, https://doi.org/10.1016/j.apenergy.2015.05.102.
[16] G.L. Plett, Extended Kalman filtering for battery management systems of LiPB-based HEV battery packs, J. Power Sources 134 (2004) 252–261, https://doi.org/10.1016/j.jpowsour.2004.02.031.
[17] G.L. Plett, Extended Kalman filtering for battery management systems of LiPB-based HEV battery packs, J. Power Sources 134 (2004) 262–276, https://doi.org/10.1016/j.jpowsour.2004.02.032.
[18] G.L. Plett, Extended Kalman filtering for battery management systems of LiPB-based HEV battery packs, J. Power Sources 134 (2004) 277–292, https://doi.org/10.1016/j.jpowsour.2004.02.033.
[19] X. Hu, S. Li, H. Peng, F. Sun, Robustness analysis of state-of-charge estimation methods for two types of Li-ion batteries, J. Power Sources 217 (2012) 209–219, https://doi.org/10.1016/j.jpowsour.2012.06.005.
[20] H. Benhammou, K. Anoune, A. Tajmouati, Optimizing state of charge estimation using thevenin models and extended Kalman filter, Discov. Electron. 2 (2025) 70, https://doi.org/10.1007/s44291-025-00106-6.
[21] H. Yu, H. Zhang, Z. Zhang, S. Yang, State estimation of lithium-ion batteries via physics-machine learning combined methods: a methodological review and future perspectives, eTransportation 24 (2025) 100420, https://doi.org/10.1016/j.etran.2025.100420.
[22] F. Stroebl, R. Petersohn, B. Schricker, F. Schaeufl, O. Bohlen, H. Palm, A multi-stage lithium-ion battery aging dataset using various experimental design methodologies, Sci. Data 11 (2024) 1020, https://doi.org/10.1038/s41597-024-03859-z.
[23] A. Pérez, I. San Martín, P. Sanchis, A. Ursúa, A novel aging modeling approach for second-life lithium-ion batteries, eTransportation 24 (2025) 100400, https://doi.org/10.1016/j.etran.2025.100400.
[24] J.-M. Timmermans, A. Nikolian, J. De Hoog, R. Gopalakrishnan, S. Goutam, N. Omar, T. Coosemans, J. Van Mierlo, A. Warnecke, D.U. Sauer, M. Swierczynski, D.I. Stroe, E. Martinez-Laserna, E. Sarasketa-Zabala, J. Gastelurrutia, N. Nerea, Batteries 2020 — lithium-ion battery first and second life ageing, validated battery models, lifetime modelling and ageing assessment of thermal parameters, in: 2016 18th European Conference on Power Electronics and Applications (EPE'16 ECCE Europe), IEEE, Karlsruhe, 2016, pp. 1–23, https://doi.org/10.1109/EPE.2016.7695698.
[25] P.V.H. Seger, P.-X. Thivel, D. Riu, A second life Li-ion battery ageing model with uncertainties: from cell to pack analysis, J. Power Sources 541 (2022) 231663, https://doi.org/10.1016/j.jpowsour.2022.231663.
[26] P.V.H. Seger, E. Coron, P.-X. Thivel, D. Riu, M. Cugnet, S. Genies, Open data model parameterization of a second-life Li-ion battery, J. Energy Storage 47 (2022) 103546, https://doi.org/10.1016/j.est.2021.103546.
[27] E. Redondo-Iglesias, M. Hassini, P. Venet, S. Pelissier, DATTES: data analysis tools for tests on energy storage, SoftwareX 24 (2023) 101584, https://doi.org/10.1016/j.softx.2023.101584.
[28] K. Zhao, Y. Liu, Y. Zhou, W. Ming, J. Wu, A hierarchical and self-evolving digital twin (HSE-DT) method for multi-faceted battery situation awareness realisation, Machines 13 (2025) 175, https://doi.org/10.3390/machines13030175.
[29] D. Salaorni, F. Bianchi, S. Colnago, A. Barisione, F. Trovò, M. Restelli, A novel digital twin for battery energy storage systems in micro-grids, J. Energy Storage 132 (2025) 117745, https://doi.org/10.1016/j.est.2025.117745.
[30] H. Xu, Q. Xu, F. Duanmu, J. Shen, L. Jin, B. Gou, F. Wu, W. Zhang, State-of-charge estimation of lithium-ion batteries based on EKF integrated with PSO-LSTM for electric vehicles, IEEE Trans. Transp. Electrific. 11 (2025) 2311–2321, https://doi.org/10.1109/TTE.2024.3421260.
[31] M. Qasem, M. Haddadin, Y. Yassin, S. Ratrout, C. Chen, S. Stoyanov, S. Al-Hallaj, M. Krishnamurthy, Real-time electrochemical model-based BMS control for mitigating Li-plating and extending battery life, IEEE Trans. Transp. Electrific. 11 (2025) 7403–7419, https://doi.org/10.1109/TTE.2025.3527899.
[32] J.N.E. Lucero, V.A. Sujan, S. Onori, An experimentally validated electro-thermal EV battery pack model incorporating cycle-life aging and cell-to-cell variations, IEEE Trans. Transp. Electrific. 10 (2024) 8122–8136, https://doi.org/10.1109/TTE.2024.3365028.
[33] H. Javaid, A. Ignjatovic, S. Parameswaran, Fidelity metrics for estimation models, in: 2010 IEEE/ACM International Conference on Computer-Aided Design (ICCAD), IEEE, San Jose, CA, USA, 2010, pp. 1–8, https://doi.org/10.1109/ICCAD.2010.5653959.